

Research Article

Simulation of Wellbore Stability during Underbalanced Drilling Operation

Reda Abdel Azim

Chemical and Petroleum Engineering Department, American University of Ras Al Khaimah, Ras Al Khaimah, UAE

Correspondence should be addressed to Reda Abdel Azim; reda.abdelazim@aurak.ac.ae

Received 13 June 2017; Accepted 2 July 2017; Published 15 August 2017

Academic Editor: Myung-Gyu Lee

Copyright © 2017 Reda Abdel Azim. This is an open access article distributed under the Creative Commons Attribution License, which permits unrestricted use, distribution, and reproduction in any medium, provided the original work is properly cited.

The wellbore stability analysis during underbalance drilling operation leads to avoiding risky problems. These problems include (1) rock failure due to stresses changes (concentration) as a result of losing the original support of removed rocks and (2) wellbore collapse due to lack of support of hydrostatic fluid column. Therefore, this paper presents an approach to simulate the wellbore stability by incorporating finite element modelling and thermoporoelastic environment to predict the instability conditions. Analytical solutions for stress distribution for isotropic and anisotropic rocks are presented to validate the presented model. Moreover, distribution of time dependent shear stresses around the wellbore is presented to be compared with rock shear strength to select appropriate weight of mud for safe underbalance drilling.

1. Introduction

Very recent studies highlighted that the wellbore instability problems cost the oil and gas industry above 500\$–1000\$ million each year [1]. The instability conditions are related to rocks response to stress concentration around the wellbore during the drilling operation. That means the rock may sustain the induced stresses and the wellbore may remain stable without collapse or failure if rock strength is enormous [2]. Factors that lead to formation instability are coming from the temperature effect (thermal) which is thermal diffusivity and the differences in temperature between the drilling mud and formation temperature. This can be described by the fact that if the drilling mud is too cold, this leads to decreasing the hoop stress. These variations in hoop stress have the same effect of tripping while drilling which generates swab and surge and may lead to both tensile and shear failure at the bottom of the well.

The interaction between the drilling fluids with formation fluid will cause pressure variation around the wellbore, which results in time dependent stresses changes locally [3]. Therefore, in this paper the interaction between geomechanics and formation fluid [4] is taken into consideration to analyze time dependent rocks deformation around the wellbore.

Another study shows that the two main effects causing collapse failure are as follows: (1) poroelastic influence of equalized pore pressure at the wellbore wall and (2) the thermal diffusion between wellbore fluids and formation fluids [3–5].

Numerous scientists presented powerful models to simulate the effect of poroelastic, thermal, and chemical effects by varying values of formation pore pressure, rock failure situation, and critical mud weight [3, 6]. These models mentioned that controlling the component of the water present in the drilling fluid results in controlling the wellbore stability. More or less, there are many parameters that could be controlled during the drilling operation as unfavorable in situ condition [7, 8]. In addition, mud weight (MW)/equivalent circulation density (ECD), mud cake (mud filtrate), hole inclination and direction, and drilling/tripping practice are considered the main parameters that affect wellbore mechanical instability [9, 10].

The factors that affect the mechanical stability are membrane efficiency, water activity interaction between the drilling fluid and shale formation, the thermal expansion, thermal diffusivity, and the differences in temperature between the drilling mud and formation temperature [11, 12].

This paper presents a realistic model to evaluate wellbore stability and predict the optimum ECD window to prevent wellbore instability problems.

2. Derivation of Governing Equation for Thermoporoelastic Model

The equations used to simulate thermoporoelastic coupling process are momentum, mass, and energy conservation. These equations are presented in detail in this section.

2.1. Momentum Conservation. The linear momentum balance equation in terms of total stresses can be written as follows:

$$\nabla \cdot \sigma + \rho g = 0, \quad (1)$$

where σ is the total stress, g is the gravity constant, and ρ is the bulk intensity of the porous media. The intensity should be written for two phases, liquid and solid, as follows:

$$\rho = \varphi \rho_l + (1 - \varphi) \rho_s. \quad (2)$$

Equation (1) can be written in terms of effective stress as follows:

$$\nabla \cdot (\sigma' - pI) + \rho g = 0, \quad (3)$$

where σ is the effective stress, p is the pore pressure, and I is the identity matrix. This equation for the stress-strain relationship does not contain thermal effects and, to include the thermoelasticity, the equation can be written as follows:

$$\sigma' = C (\varepsilon - \alpha_T \Delta T \times I), \quad (4)$$

where C is the fourth-order stiffness tensor of material properties, ε is the total strain, α_T is the thermal expansion coefficient, and ΔT is the temperature difference. The isotropic elasticity tensor C is defined as

$$C = \lambda \delta_{ij} \delta_{kl} + 2G \delta_{ik} \delta_{jl}, \quad (5)$$

where δ is the Kronecker delta and λ is the Lamé constant. G is the shear modulus of elasticity. The constitutive equation for the total strain-displacement relationship is defined as follows:

$$\varepsilon = \frac{1}{2} (\nabla \vec{u} + (\nabla \vec{u})^T), \quad (6)$$

where \vec{u} is the displacement vector and ∇ is the gradient operator.

2.2. Mass Conservation. The fluid flow in deformable and saturated porous media can be described by the following equation:

$$S_s \frac{\partial p}{\partial t} + \beta \nabla \cdot \left(\frac{\partial \vec{u}}{\partial t} \right) + \nabla \cdot q - \alpha_T \frac{\partial T}{\partial t} = Q, \quad (7)$$

where β is the Biots coefficient and assumed to be = 1.0 in this study, p is the pore fluid pressure, T is the temperature, α_T is

the thermal expansion coefficient, q is the fluid flux, and Q is the sink/source, and S_s is the specific storage which is defined by

$$S_s = \left(\frac{1 - \varphi}{K_s} \right) + \left(\frac{\varphi}{K_l} \right), \quad (8)$$

where K_s is the compressibility of solid and K_l is the compressibility of liquid. The fluid flux term (q) in the mass balance in (7) can be described by using Darcy's flow equation because the intensity has been assumed constant in this study:

$$q = -\frac{k}{\mu} (\nabla p - \rho \vec{g}), \quad (9)$$

where k is the permeability of the domain. The Cubic law is used in determining fracture permeability.

2.3. Energy Conservation. The energy balance equation for heat transport through porous media can be described as follows:

$$(\rho c_p)_{\text{eff}} \frac{\partial T}{\partial t} + \nabla \cdot q_T = Q_T, \quad (10)$$

where q_T is the heat flux, Q^T is the heat sink/source term, and ρc_p is the heat storage and equals

$$(\rho c_p)_{\text{eff}} = \varphi (c_p \rho)_{\text{liquid}} + (1 - \varphi) (c_p \rho)_{\text{solid}}. \quad (11)$$

In this study, conduction and convection heat transfers are considered during numerical simulation. The heat flux term in (10) can be written as

$$q_T = -\lambda_{\text{eff}} \nabla T + (c_p \rho)_{\text{liquid}} v \cdot T, \quad (12)$$

where v is the velocity of the fluid. The first term on the right hand side of (12) is the conduction term and the second term is the convective heat transfer term and λ_{eff} is the effective heat conductivity of the porous medium, which can be defined as

$$\lambda_{\text{eff}} = \varphi \lambda_{\text{liquid}} + (1 - \varphi) \lambda_{\text{solid}}. \quad (13)$$

2.4. Discretization of the Equations. First one discretizes the thermoporoelastic governing equations by using Greens' theorem [13] to derive equations weak formulations. The weak form of mass, energy, and momentum balance in (1), (7), and (10) can be written as follows, respectively:

$$\begin{aligned} & \int_{\Omega} w S_s \frac{\partial p}{\partial t} d\Omega + \int_{\Omega} w^T \alpha \nabla \cdot \frac{\partial \vec{u}}{\partial t} d\Omega + \int_{\Omega} w \beta \frac{\partial T}{\partial t} \\ & - \int_{\Omega} \nabla w^T \cdot q_H d\Omega + \int_{\Gamma_H^q} w (q_H \cdot n) d\Gamma \\ & - \int_{\Omega} w Q_H d\Omega = 0, \end{aligned} \quad (14)$$

$$\int_{\Gamma_d} w b_m S_s \frac{\partial p}{\partial t} d\Gamma + \int_{\Gamma_d} w \alpha \frac{\partial b_m}{\partial t} d\Gamma + \int_{\Gamma_d} w \beta \frac{\partial T}{\partial t} d\Gamma - \int_{\Gamma_d} \nabla w^T \cdot (b_h q_H) d\Omega + \int_{\Gamma_H^q} w b_h (q_H \cdot n) d\Gamma \quad (15)$$

$$+ \int_{\Gamma_d} w q_H^+ d\Gamma + \int_{\Gamma_d} w q_H^- d\Gamma = 0,$$

$$\int_{\Omega} w c_p \rho \frac{\partial T}{\partial t} d\Omega + \int_{\Omega} w c_p \rho q_H \cdot \nabla T d\Omega - \int_{\Omega} \nabla w^T \cdot (-\lambda \nabla T) d\Omega + \int_{\Gamma_T^q} w (-\lambda \nabla T \cdot n) d\Gamma \quad (16)$$

$$- \int_{\Omega} w^T Q_T d\Omega = 0,$$

$$\int_{\Gamma_d} w b_m c_p \rho^l \frac{\partial T}{\partial t} d\Gamma + \int_{\Gamma_d} w c_p \rho^l b_h q_H \cdot \nabla T d\Gamma - \int_{\Gamma_d} \nabla w^T \cdot (-b_m \lambda^l \nabla T) d\Gamma \quad (17)$$

$$+ \int_{\Gamma_T^q} w (-b_m \lambda^l \nabla T \cdot n) d\Gamma + \int_{\Gamma_d} w q_T^+ d\Gamma$$

$$+ \int_{\Gamma_d} q_T^- d\Gamma = 0,$$

$$\int_{\Omega} \nabla^s w^T \cdot (\sigma' - \alpha p I) d\Omega - \int_{\Omega} w^T \cdot \rho g d\Omega - \int_{\Gamma_t} w^T \cdot \vec{t} d\Gamma - \int_{\Gamma_d} w^{+T} \cdot \vec{t}_d^+ d\Gamma \quad (18)$$

$$- \int_{\Gamma_t} w^{-T} \cdot \vec{t}_d^- d\Gamma = 0,$$

where w is the test function, Ω is the model domain, Γ is the domain boundary, t is the traction vector, superscripts $+/-$ refer to the value of the corresponding parameters on opposite sides of the fracture surfaces, respectively, S_s is the specific storage, n is the porosity, q_H is the volumetric Darcy flux, β is the thermal expansion coefficient, Q_H is the fluid sink/source term between the fractures, q_T is the heat flux, c_p is the specific heat capacity, b_m and b_h are mechanical and hydraulic fracture apertures, Q_T is the heat sink/source term, α is the thermal expansion coefficient, λ is the thermal conductivity, and d refers to the fracture plane.

Then the Galerkin method is used to spatially discretize the weak forms of (14) to (18). The primary variables of the field problem are pressure p , temperature T , and displacement vector u . All of these variables are approximated by using the interpolation function in finite element space as follows:

$$\begin{aligned} u &= N_u \bar{u}, \\ p &= N_p \bar{p}, \\ T &= N_T \bar{T}, \end{aligned} \quad (19)$$

TABLE 1: Reservoir inputs used for validation of poroelastic numerical model using circular homogenous reservoir.

Parameter	Value
Poisson ratio	0.2
Young's modulus	40 GPa
Maximum horizontal stress	40 MPa (5800 psi)
Minimum horizontal stress	37.9 MPa (5500 psi)
Wellbore pressure (P_w)	6.89 MPa (1000 psi)
Initial reservoir pressure (P_i)	37.9 MPa (5500 psi)
Fluid bulk module (K_f)	2.5 GPa
Fluid compressibility	$1.0 \times 10^{-5} \text{ Pa}^{-1}$
Biot's coefficient	1.0
Fluid viscosity	$3 \times 10^{-4} \text{ Pa}\cdot\text{s}$
Matrix permeability	$9.869 \times 10^{-18} \text{ m}^2$ (0.01 md)
Wellbore radius	0.1 m
Reservoir outer radius	1000 m

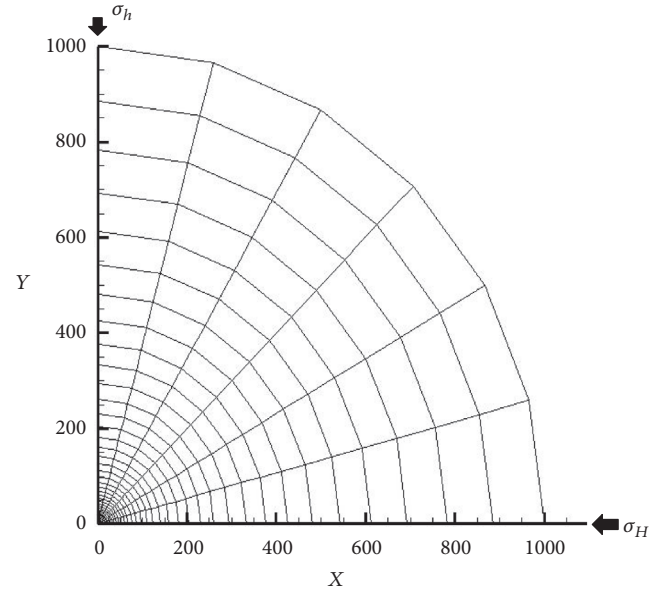


FIGURE 1: Two-dimensional circular reservoir shape used for validation of poroelastic numerical model with $\sigma_H = 39.9 \text{ MPa}$ and $\sigma_v = 37.9 \text{ MPa}$, $P_r = 37.9 \text{ MPa}$, and $\Delta p = 31 \text{ MPa}$.

where N is the corresponding shape function and \bar{u} , \bar{p} , and \bar{T} are the nodal unknowns values.

3. Validation of Poroelastic Numerical Model

The verification of poroelastic numerical model against analytical solutions (see Appendix) is presented in this section. A two-dimensional model of circular shaped reservoir with an intact wellbore of 1000 m drainage radius and 0.1 m wellbore radius is used (see Figure 1). The reservoir input data used are presented in Table 1. The numerical model is initiated with drained condition obtained by using Kirsch's problem [14]. These conditions with the analytical solution equations for

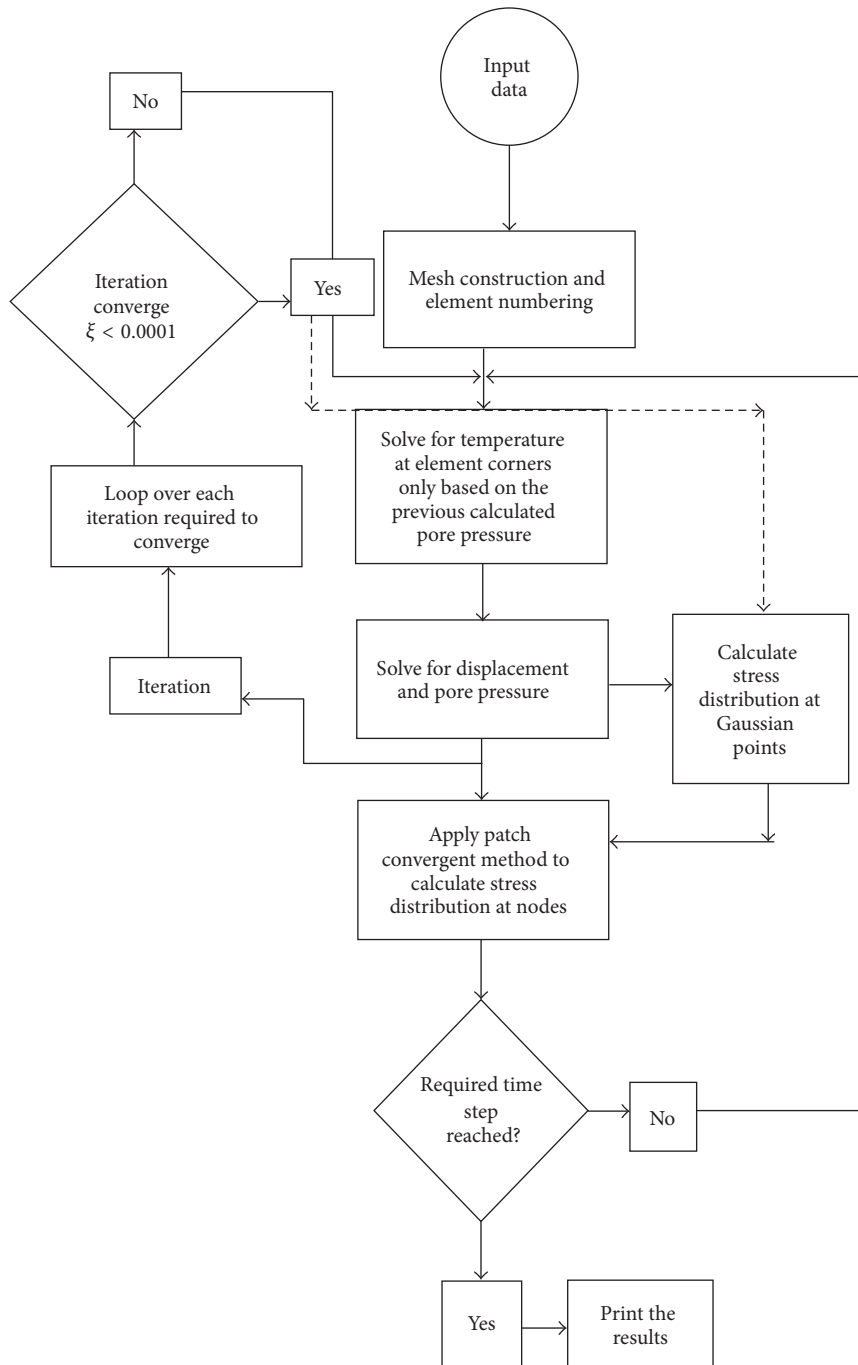


FIGURE 2: Flow chart describes how the nodal unknowns are solved using iterations process.

drained condition for the given pore pressure, displacement, and stresses [15, 16] are presented in the Appendix. Flow chart describes the solution process for pressure and displacement for poroelastic model and also for temperature for thermoporoelastic frameworks is presented in Figure 2. The numerical results obtained are plotted against the analytical solutions in Figures 3–6.

For the verification purpose, a number of assumptions are made.

Initial State. In this study, zero time (initial state) is assumed to represent drained situation in which pore pressure is stabilized.

Boundary Conditions. They are boundary conditions for the poroelastic model in this model.

Rock and Fluid Properties. In the numerical model, Young's modulus, Poisson's ratio, porosity, permeability, and total system compressibility as well as viscosity of fluid are assumed

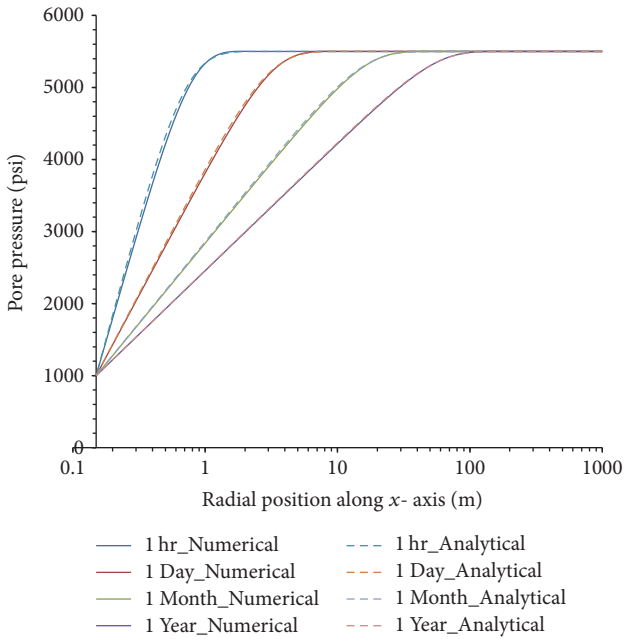


FIGURE 3: Pore pressure as a function of radius and time in poroelastic medium with $\sigma_H = 5800$ psi and $\sigma_h = 5500$ psi, $P_r = 5500$ psi, $P_w = 1000$ psi, $k_x = 0.01$ md, and $k_y = 0.01$ md.

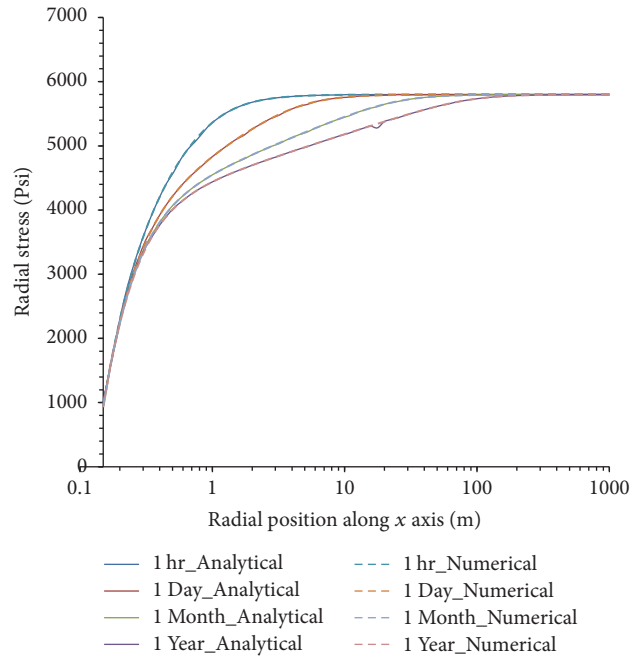


FIGURE 5: X-component of radial stresses as a function of time in poroelastic medium with $\sigma_H = 5800$ psi and $\sigma_h = 5500$ psi, $P_r = 5500$ psi, $P_w = 1000$ psi, $k_x = 0.01$ md, and $k_y = 0.01$ md.

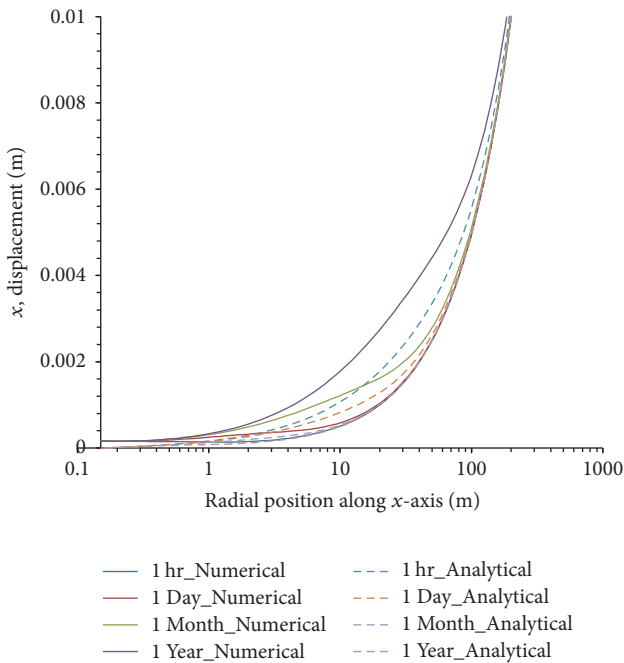


FIGURE 4: X-displacement along x-axis as a function of time in poroelastic medium with $\sigma_H = 5800$ psi and $\sigma_h = 5500$ psi, $P_r = 5500$ psi, $P_w = 1000$ psi, $k_x = 0.01$ md, and $k_y = 0.01$ md.

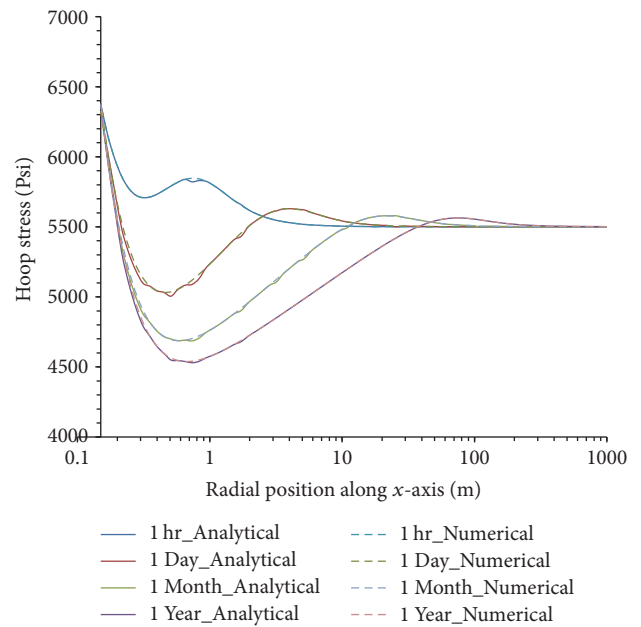


FIGURE 6: X-component of tangential stresses as a function of time in poroelastic medium with $\sigma_H = 5800$ psi and $\sigma_h = 5500$ psi, $P_r = 5500$ psi, $P_w = 1000$ psi, $k_x = 0.01$ md, and $k_y = 0.01$ md.

to be independent of time and space in order to be consistent with the analytical solutions.

As can be seen from Figure 3, the numerical results match well with the analytical solutions. Due to discontinuity of initial state and the first time step in the numerical procedure a small mismatch is observed between numerical

and analytical solutions for $t = 1$ hr. It is evident that, for an initial drained condition and horizontal permeability anisotropy, no directional dependence of the change in pore pressure is observed despite the anisotropic horizontal stress state.

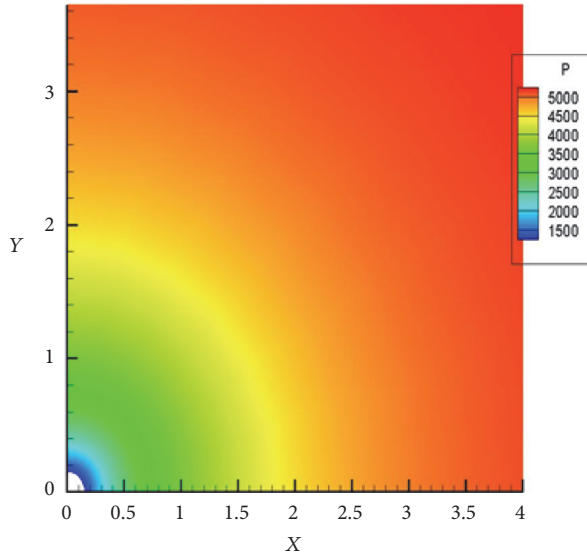


FIGURE 7: Pore pressure contour map after 1 hr of fluid production (for near-wellbore region) with $\sigma_H = 5800$ psi and $\sigma_h = 5500$ psi, $P_r = 5500$ psi, $P_w = 1000$ psi, $k_x = 0.01$ md, and $k_y = 0.01$ md.

In Figure 4 the numerical results for displacement have a small mismatch with the analytical solutions. This is due to the method (Patch Recovery Method) that has been used to distribute initial reservoir displacement and calculating the change in in situ stresses with time.

In Figure 5, the numerical results show a good agreement with the exact solutions for different time and orientations. For all cases, as expected, σ_x approaches the maximum horizontal in situ stress (5800 psi) at far field (away from wellbore). The discontinuity of σ_x at wellbore wall is due to the imposed pressure boundary condition. It is assumed that wellbore pressure is equal to the reservoir pressure at zero time in order to simulate drained initial state. It is also observed that as time progresses, the size of the area, which is affected by the change in σ_x , increases. This is due to change in pore pressure.

In Figure 6 numerical results of σ_y match well with that of the analytical solutions for different time. As expected, σ_y approaches the minimum horizontal in situ stress (5500 psi) at far field (away from wellbore).

The results of pore pressure and effective stress after one hour of production are presented in Figures 7–9 in reservoir entire region. These figures (Figures 7–9) clarify how the pressure and stresses are changing from the wall of the wellbore to the reservoir boundary.

4. Failure Criteria

Shear failure will occur if

$$\sigma'_3 < -T_0, \quad (20)$$

where σ'_3 the lowest principle is effective stress and T_0 is the rock tensile strength.

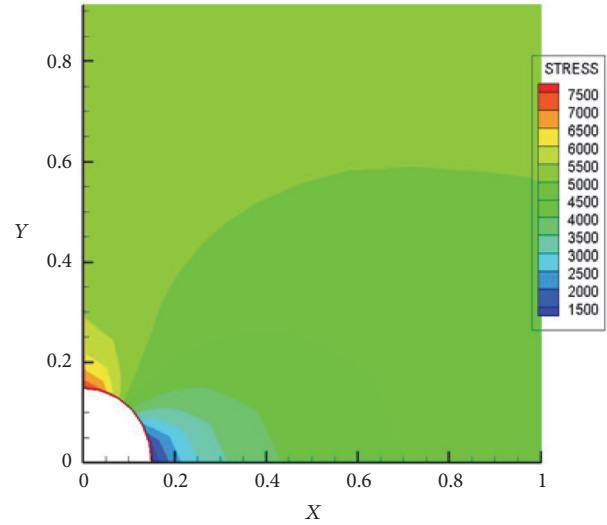


FIGURE 8: X-component of radial stresses contour map after 1 hr of fluid production (for near-wellbore region) with $\sigma_H = 5800$ psi and $\sigma_h = 5500$ psi, $P_r = 5500$ psi, $P_w = 1000$ psi, $k_x = 0.01$ md, and $k_y = 0.01$ md.

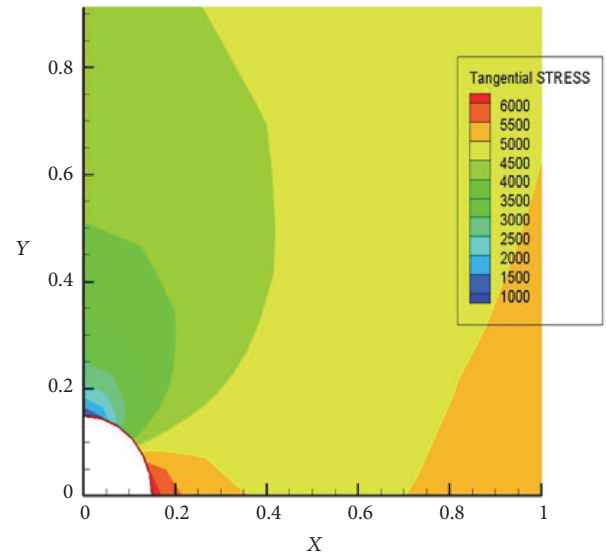


FIGURE 9: X-component of tangential stresses contour map after 1 hr of fluid production (for near-wellbore region) with $\sigma_H = 5800$ psi and $\sigma_h = 5500$ psi, $P_r = 5500$ psi, $P_w = 1000$ psi, $k_x = 0.01$ md, and $k_y = 0.01$ md.

Using Mohr-Coulomb criteria, shear failure criteria are met when

$$\tau_{\text{net}} = \frac{1}{2 \cos \varphi} (\sigma'_1 (1 - \sin \varphi) - \sigma'_3 (1 + \sin \varphi)) > S_0, \quad (21)$$

where σ'_1 is the highest principle effective stress, τ_{net} is the net shear stress, φ is the angle of internal friction, and S_0 is the rock shear strength. Once the maximum principle stress surpasses the rock shear strength, rock failure takes place at the wellbore. Therefore, evaluating the highest principle stress

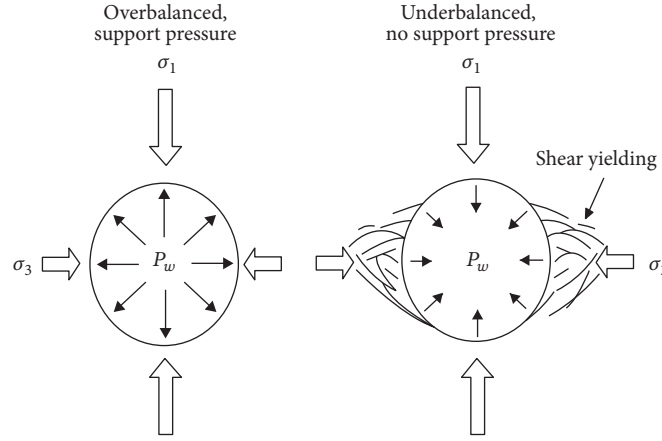


FIGURE 10: Shear yielding occurs for underbalanced conditions due to the absence of a support pressure on the borehole wall [16].

is important criterion to predict rock failure for analysis of wellbore stability [16].

Drilling with underbalanced technique where the bottom-hole pressure is lower than the formation pore pressure regularly promotes borehole instability. Thus, it is important to design and determine the ideal range of the bottom-hole pressure during underbalanced drilling operation, to avoid generating hydraulic fractures, differential sticking, or undesirable level of formation damage [17] (see Figure 10).

5. Case Study

This test case has been taken from a field located in southern part of Iran. The operator is considered a well drilled at an approximate depth of 4000 ft. the recorded pore pressure gradient from the DST test analysis is 7.7 lb/gal. The rock mechanical data used for wellbore stability analysis are determined from triaxial test on core samples and presented in Table 2. The wellbore stability analysis has been executed using underbalance technique. Therefore, the reduction in pore pressure during the drilling process will directly affect the horizontal and shear stresses. To avoid either loss of circulation problems or borehole failure, the mud pressure should be less than the formation fracture pressure and greater than its collapse pressure. Therefore, it is mandatory to predict the changes of stresses values as reservoir pressure drops. In this case study, the mud weight recommended to be used is 5 lb/gal.

To do this analysis, a finite element mesh has been generated as the one presented in Figure 1 and it was refined around the wellbore. The boundary conditions have been assigned to the model and Mohr-Coulomb criteria [18] are used for the simulation to predict the stresses and pore pressure distribution with time around the wellbore.

6. Results and Discussion

Breakout shear failure occurred during underbalance drilling operation; therefore, it is very important to predict the failure at the wellbore wall using failure criteria. Because of pore

TABLE 2: Case study input data.

<i>Mechanical parameters</i>	
Poisson ratio (ν)	0.2
Bulk Young's modulus (E)	4.4 GPa
Maximum horizontal stress (σ_H)	16.8 MPa (2436 psi)
Minimum horizontal stress (σ_h)	14 MPa (2030 psi)
Wellbore pressure (P_w)	6.89 MPa (1000 psi)
<i>Hydraulic parameters</i>	
Initial reservoir pressure (P_i)	11.1 MPa (1610 psi)
Fluid bulk module (K_f)	0.45 GPa
Fluid compressibility	$1.0 \times 10^{-5} \text{ Pa}^{-1}$
Biot's coefficient	1.0
<i>Physical parameters</i>	
Fluid viscosity	$3 \times 10^{-4} \text{ Pa}\cdot\text{s}$
Fluid density	1111 kg/m^3
Matrix permeability	$9.869 \times 10^{-18} \text{ m}^2$ (0.01 md)
Porosity (ϕ)	0.1
Wellbore radius	0.15 m
Reservoir outer radius	1000 m
Formation temperature (T_f)	375 °K
Drilling mud temperature (T_m)	330 °K
Thermal osmosis coefficient (K^T)	$1 \times 10^{-11} \text{ m}^2/\text{s K}$
Thermal expansion coefficient of fluid (α^f)	$3 \times 10^{-4} 1/\text{K}$
Thermal diffusivity (C^T)	$1.1 \times 10^{-6} \text{ m}^2/\text{s}$
Thermal expansion coefficient of solid (α^s)	$1.8 \times 10^{-5} 1/\text{K}$

pressure dissipation, the failure becomes time dependent as the net shear stress increases with time at the borehole wall.

It can be seen from Figure 11 that the net shear stress is the lowest for the time before starting of the underbalance drilling operation. Then, at the wellbore wall, it can be noticed that the net shear stress drops suddenly after 4 s of the drilling operation. In addition, at this time, the net shear stress value is higher than net shear stress for long time of the drilling

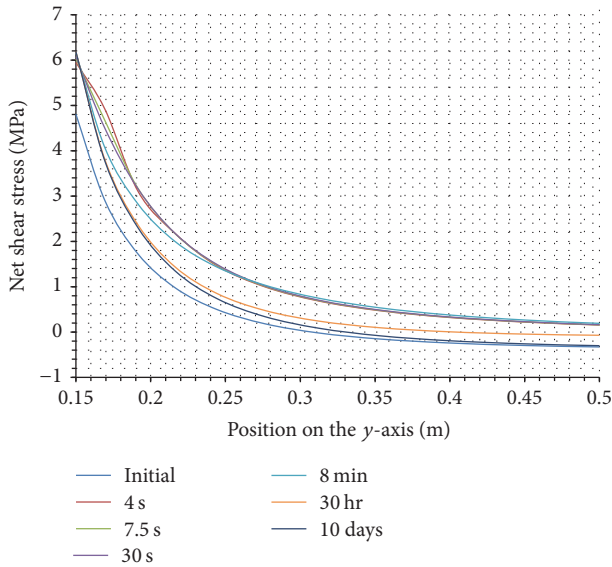


FIGURE 11: Y-component of net shear stresses as a function of time in poroelastic medium with $\sigma_H = 16.8$ MPa and $\sigma_h = 14$ MPa, $P_r = 11$ MPa, $P_w = 9.7$ MPa, $k_x = 0.01$ md, $k_y = 0.01$ md, and $T_m = 330$ K.

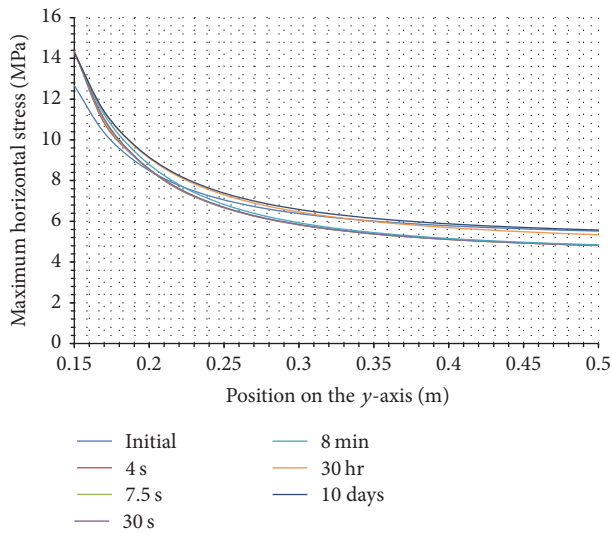


FIGURE 12: Y-component of maximum horizontal stresses as a function of time in poroelastic medium with $\sigma_H = 16.8$ MPa and $\sigma_h = 14$ MPa, $P_r = 11$ MPa, $P_w = 9.7$ MPa, $k_x = 0.01$ md, $k_y = 0.01$ md, and $T_m = 330$ K.

operation. This effect of short time of drilling operation on the net shear stress value is uncertain, as this time may be too short to allow failure to be devolved. But, in this case study, by comparing the net shear stress value with the rock shear strength, we found its value lower than the rock shear strength (14 MPa). This proves that the failure will not occur using mud weight of 5 lb/gal. Figures 12, 13, and 14 show y -stresses at the wellbore wall.

Distribution of the net shear stress along y -axis for the cooling ($T_m < T_f$) effect of mud during the underbalance drilling operation is presented in Figure 15. From this figure,

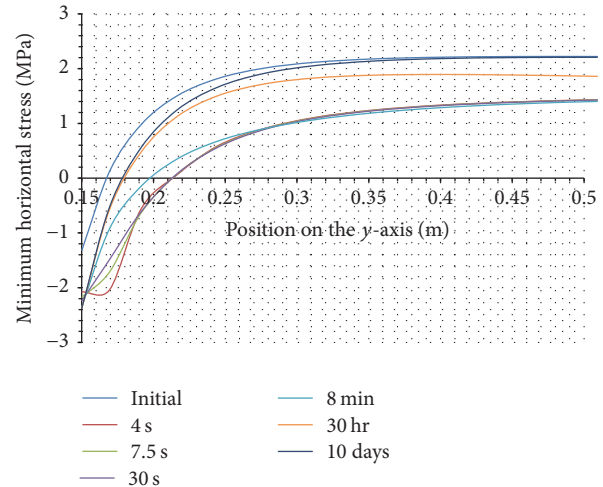


FIGURE 13: Y-component of minimum horizontal stresses as a function of time in poroelastic medium with $\sigma_H = 16.8$ MPa and $\sigma_h = 14$ MPa, $P_r = 11$ MPa, $P_w = 9.7$ MPa, $k_x = 0.01$ md, $k_y = 0.01$ md, and $T_m = 330$ K.

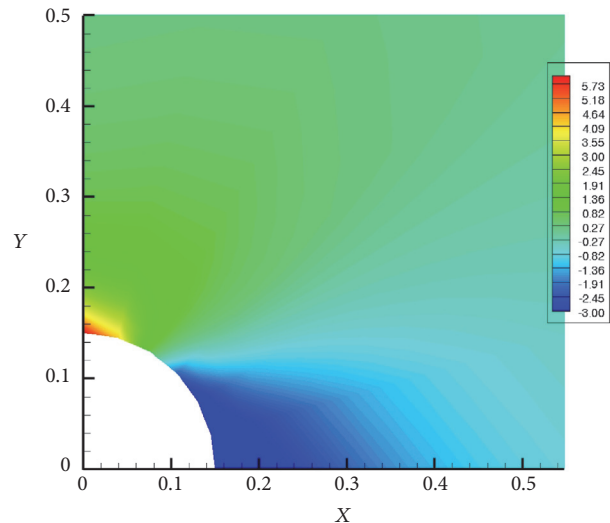


FIGURE 14: Y-component of net shear stresses at $t = 30$ s in poroelastic medium with $\sigma_H = 16.8$ MPa and $\sigma_h = 14$ MPa, $P_r = 11$ MPa, $P_w = 9.7$ MPa, $k_x = 0.01$ md, $k_y = 0.01$ md, and $T_m = 330$ K.

it can be seen that the net shear stress accumulated at the wellbore wall and increases the probability of failure of the well. If the breakout occurs, it will initiate near the wellbore not at the wall bore wall (see Figure 15). If there is a breakout, the shear forces will cause rock to fall into the wellbore and in this case the well status becomes unstable (wellbore instability). But, in this case study, the net shear stress is too low to cause failure and this well will not suffer from instability problems even for long drilling period. Figures 16, 17, and 18 show y -stresses at the wellbore wall with the effect of mud cooling.

The cooling process near the wellbore can alter the stresses significantly and leads to increasing the total stresses and the pore pressure drop inside the formation; those

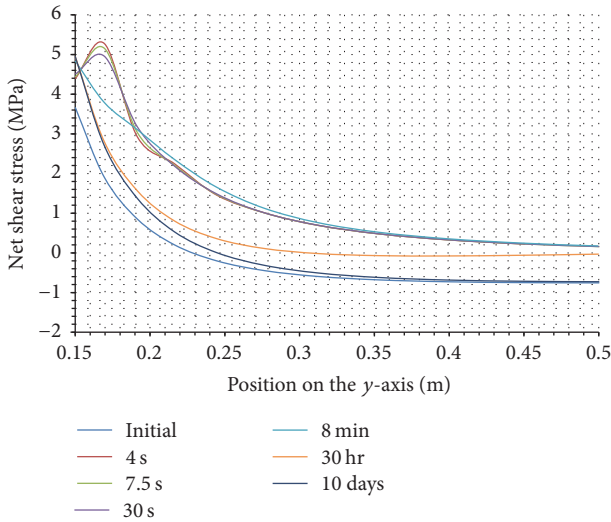


FIGURE 15: Y-component of net shear stresses as a function of time in poroelastic medium with $\sigma_H = 16.8$ MPa and $\sigma_h = 14$ MPa, $P_r = 11$ MPa, $P_w = 9.7$ MPa, $k_x = 0.01$ md, $k_y = 0.01$ md, and $T_m = 300$ K.

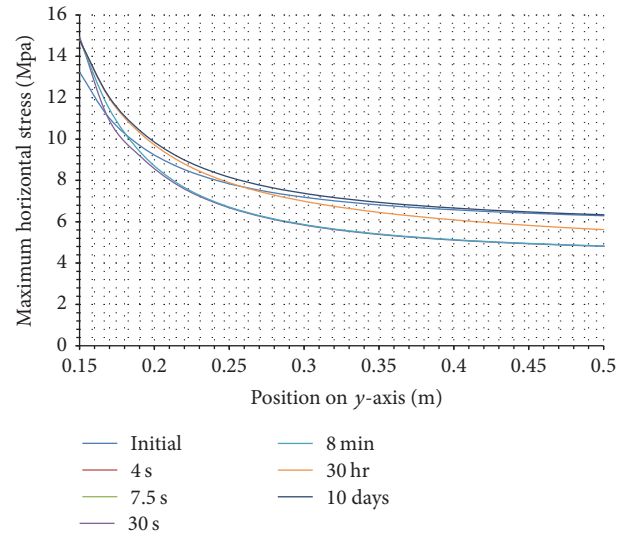


FIGURE 17: Y-component of maximum horizontal stresses as a function of time in poroelastic medium with $\sigma_H = 16.8$ MPa and $\sigma_h = 14$ MPa, $P_r = 11$ MPa, $P_w = 9.7$ MPa, $k_x = 0.01$ md, $k_y = 0.01$ md, and $T_m = 300$ K.

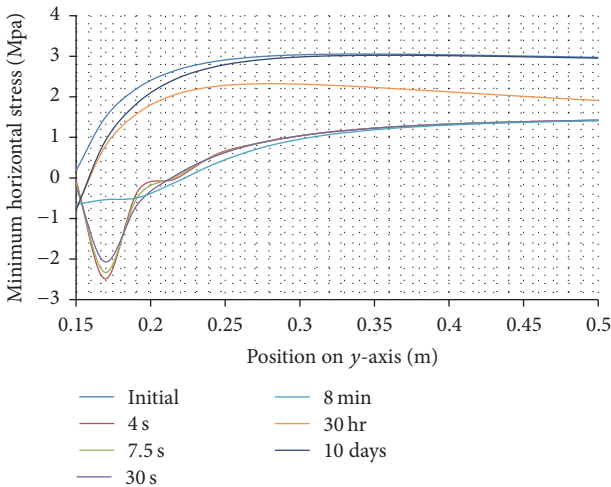


FIGURE 16: Y-component of minimum horizontal stresses as a function of time in poroelastic medium with $\sigma_H = 16.8$ MPa and $\sigma_h = 14$ MPa, $P_r = 11$ MPa, $P_w = 9.7$ MPa, $k_x = 0.01$ md, $k_y = 0.01$ md, and $T_m = 300$ K.

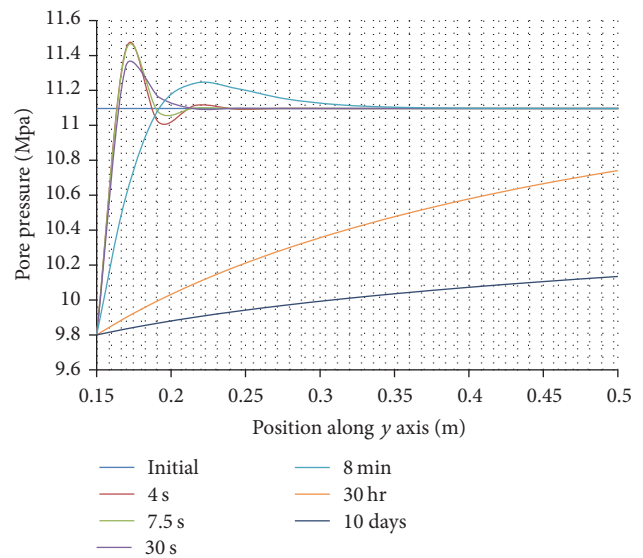


FIGURE 18: Pore pressure as a function of radius and time in poroelastic medium with $\sigma_H = 16.8$ MPa and $\sigma_h = 14$ MPa, $P_r = 11$ MPa, $P_w = 9.7$ MPa, $k_x = 0.01$ md, $k_y = 0.01$ md, and $T_m = 300$ K.

increasing in total stresses and pore pressure cause increasing in the effective stresses near the wellbore (see Figures 15, 17, and 18). As time increases, the mud temperature will equilibrate with its surroundings so that the formations higher in the section being drilled are subjected to the increased temperature of the mud. Heating process leads to reducing the pore pressure and net shear stresses near the wellbore (see Figures 11 and 13).

The formation cooling increases the pore pressure (see Figure 19) near the wellbore wall at the beginning of the drilling operation (for 4 s, 7.5 s, and 30 s). This is due to thermal osmosis process that results in fluid movement out

of the formation. Then, the transient response causes pore pressure on the y-axis to decrease.

Figure 20 shows a relationship between the mud weight and accumulated shear stress around the wellbore. It can be seen from the figure that, with using mud weight of 7.5 ppg, the net shear stress (16 MPa) becomes greater than the rock strength (14 MPa). Therefore, to avoid wellbore breakouts, Mohr-Coulomb failure criterion indicates that the safe mud weight used in this case study is between 5.5 and 7.5 ppg.

TABLE 3: General description of the problem.

Inner boundary	Outer boundary	Wellbore pressure	Pore pressure	Maximum horizontal stress	Minimum horizontal stress
r_w	$r_e = \infty$	P_w	$P = P_{int}$	σ_H	σ_h

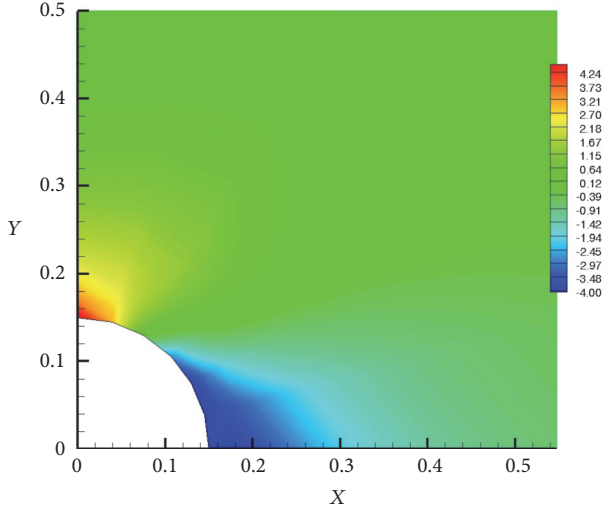


FIGURE 19: Y-component of net shear stresses at $t = 30$ s in poroelastic medium with $\sigma_H = 2436$ psi and $\sigma_h = 2030$ psi, $P_r = 1610$ psi, $P_w = 1421$ psi, $k_x = 0.01$ md, $k_y = 0.01$ md, and $T_m = 300$ K.

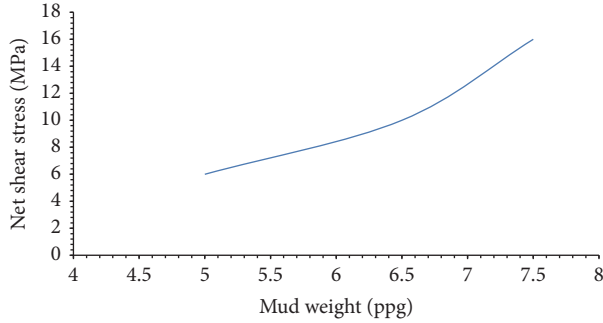


FIGURE 20: Relationship between mud weight and net shear stress (iteration process).

7. Conclusion

An integrated thermoporoelastic numerical model has been presented in this paper to predict the stresses distribution and the instability problem around the wall of the wellbore. The model has been validated against the analytical model.

Behaviour of the stresses around the wellbore in underbalance drilling operation is very sensitive to the mud weight and mechanical properties of the rock as well. The pore pressure and stresses around the wellbore are significantly affected by the thermal effects. Thus, when the mud temperature is lower than the formation temperature, the pore pressure changes, and the net shear stresses values are increased around the wellbore which increase the probability

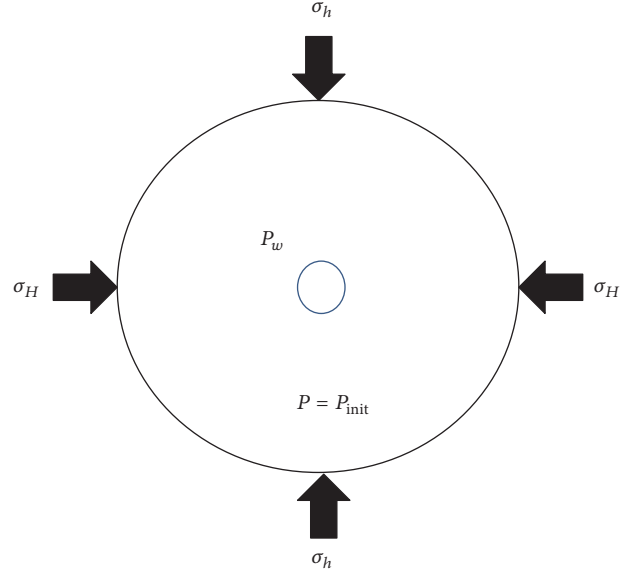


FIGURE 21: Schematic of the problem.

of occurrence of the instability problem, if its values become greater than the rock shear strength.

Appendix

Elastic Deformation of a Pressurized Wellbore in a Drained Rock Subjected to Anisotropic In Situ Horizontal Stress (Kirsch's Problem)

General description of the problem is tabulated in Table 3 and schematic of the problem is illustrated in Figure 21. This problem accounts for the concept of effective stress.

(i) Analytical pressure is

$$p(r, t) = p_i + (p_w - p_i) g(r, t). \quad (\text{A.1})$$

(ii) Analytical radial stress is

$$\begin{aligned} \sigma_{rr}(r, \theta) = & \frac{\sigma_H + \sigma_h}{2} \left(1 - \frac{r_w^2}{r^2} \right) \\ & + \frac{\sigma_H - \sigma_h}{2} \left(1 + 3 \frac{r_w^4}{r^4} - 4 \frac{r_w^2}{r^2} \right) \cos(2\theta) \quad (\text{A.2}) \\ & + P_w \frac{r_w^2}{r^2} + 2\eta (p_w - p_i) \frac{r_w}{r} h(r, t). \end{aligned}$$

(iii) Analytical tangential stress is

$$\begin{aligned} \sigma_{\theta\theta}(r, \theta) = & \frac{\sigma_H + \sigma_h}{2} \left(1 + \frac{r_w^2}{r^2} \right) \\ & - \frac{\sigma_H - \sigma_h}{2} \left(1 + 3 \frac{r_w^4}{r^4} \right) \cos(2\theta) \\ & - p_w \frac{r_w^2}{r^2} \\ & - 2\eta(p_w - p_i) \left(\frac{r_w}{r} h(r, t) + g(r, t) \right), \end{aligned} \quad (\text{A.3})$$

$$\tilde{g}(r, s) = \frac{K_0(\xi)}{sK_0(\beta)},$$

$$\tilde{h}(r, s) = \frac{1}{s} \left[\frac{K_1(\xi)}{\beta K_0(\beta)} - \frac{r_w}{r} \frac{K_1(\beta)}{\beta K_0(\beta)} \right].$$

(iv) Radial displacement is

$$\begin{aligned} u_r(r, \theta) = & \frac{r}{4G} (\sigma'_H + \sigma'_h) \left(1 - 2\nu + \frac{r_w^2}{r^2} \right) \\ & + \frac{r}{4G} (\sigma'_H - \sigma'_h) \\ & \times \left(\frac{r_w^2}{r^2} \left(4 - 4\nu - \frac{r_w^2}{r^2} \right) + 1 \right) \cos(2\theta) \\ & - \frac{p'_w r_w^2}{2G r} - \frac{\eta}{G} r_w (p_w - p_i) h(r, t). \end{aligned} \quad (\text{A.4})$$

(v) Tangential displacement is

$$\begin{aligned} u_\theta(r, \theta) = & -\frac{r}{4G} (\sigma'_H - \sigma'_h) \\ & \cdot \left(\frac{r_w^2}{r^2} \left(2 - 4\nu - \frac{r_w^2}{r^2} \right) + 1 \right) \sin(2\theta). \end{aligned} \quad (\text{A.5})$$

(vi) Analytical temperature is

$$T(r, t) = T_o + (T_w - T_o) L^{-1} \left\{ \frac{1}{s} \frac{K_0(r\sqrt{s/c_0})}{K_0(r_w\sqrt{s/c_0})} \right\}, \quad (\text{A.6})$$

where \tilde{g} is the Laplace transformation of g and

$$\begin{aligned} \xi &= r \sqrt{\frac{s}{c}}, \\ \beta &= r_w \sqrt{\frac{s}{c}}, \end{aligned} \quad (\text{A.7})$$

and K_0 and K_1 are the first-order modified Bessel function of the first and second kind. Laplace inversion is solved using the method presented by Detournay and Cheng [15]. The solution in time is achieved by the following formula.

The Laplace transformation can be inverted using

$$f(r, t) \approx \frac{\ln 2}{t} \sum_{n=1}^N C_n \tilde{f} \left(r, n \frac{\ln 2}{t} \right), \quad (\text{A.8})$$

where (\ln) represents the natural logarithm and

$$C_n = (-1)^{n+N/2} \cdot \sum_{k=[(n+1)/2]}^{\min(n, N/2)} \frac{k^{N/2} (2k)!}{(N/2 - k)! k! (k-1)! (n-k)! (2k-n)!}. \quad (\text{A.9})$$

Conflicts of Interest

The author declares that he has no conflicts of interest.

References

- [1] S. Rafieepour, C. Ghotbi, and M. R. Pishvaie, "The effects of various parameters on wellbore stability during drilling through shale formations," *Petroleum Science and Technology*, vol. 33, no. 12, pp. 1275–1285, 2015.
- [2] G. Chen, M. E. Chenevert, M. M. Sharma, and M. Yu, "A study of wellbore stability in shales including poroelastic, chemical, and thermal effects," *Journal of Petroleum Science and Engineering*, vol. 38, no. 3-4, pp. 167–176, 2003.
- [3] H. Roshan and S. S. Rahman, "Analysis of pore pressure and stress distribution around a wellbore drilled in chemically active elastoplastic formations," *Rock Mechanics and Rock Engineering*, vol. 44, no. 5, pp. 541–552, 2011.
- [4] M. Hodge, K. L. Valencia, Z. Chen, and S. S. Rahman, "Analysis of time-dependent wellbore stability of underbalanced wells using a fully coupled poroelastic model," in *Proceedings of the SPE Annual Technical Conference and Exhibition, ATCE 2006: Focus on the Future*, pp. 3274–3278, September 2006.
- [5] M. Gomar, I. Goodarzania, and S. R. Shadizadeh, "A transient fully coupled thermo-poroelastic finite element analysis of wellbore stability," *Arabian Journal of Geosciences*, vol. 8, no. 6, pp. 3855–3865, 2014.
- [6] M. Aslannezhad, A. Khaksar manshad, and H. Jalalifar, "Determination of a safe mud window and analysis of wellbore stability to minimize drilling challenges and non-productive time," *Journal of Petroleum Exploration and Production Technology*, vol. 6, no. 3, pp. 493–503, 2016.
- [7] S. Salehi, G. Hareland, and R. Nygaard, "Numerical simulations of wellbore stability in under-balanced-drilling wells," *Journal of Petroleum Science and Engineering*, vol. 72, no. 3-4, pp. 229–235, 2010.
- [8] W. K. Heiduc and S.-W. Wong, "Hydration swelling of water-absorbing rocks: a constitutive model," *International Journal for Numerical and Analytical Methods in Geomechanics*, vol. 20, no. 6, pp. 403–430, 1996.
- [9] P. McLellan and C. Hawkes, "Borehole stability analysis for underbalanced drilling," *Journal of Canadian Petroleum Technology*, vol. 40, no. 5, pp. 31–38, 2001.
- [10] M. R. McLean and M. A. Addis, "Wellbore stability: the effect of strength criteria on mud weight recommendations," in *Proceedings of the SPE Annual Technical Conference and Exhibition*, pp. 9–17, September 1990.

- [11] M. F. Kanfar, Z. Chen, and S. S. Rahman, "Risk-controlled wellbore stability analysis in anisotropic formations," *Journal of Petroleum Science and Engineering*, vol. 134, pp. 214–222, 2015.
- [12] T. Ma and P. Chen, "A wellbore stability analysis model with chemical-mechanical coupling for shale gas reservoirs," *Journal of Natural Gas Science and Engineering*, vol. 26, pp. 72–98, 2015.
- [13] S. De and K. J. Bathe, "The method of finite spheres," *Computational Mechanics*, vol. 25, no. 4, pp. 329–345, 2000.
- [14] G. Kirsch, "Theory of elasticity and application in strength of materials," *Zeitschrift des Vereins Deutscher Ingenieure*, vol. 42, no. 29, pp. 797–807, 1898.
- [15] E. Detournay and A.-D. Cheng, "Poroelastic response of a borehole in a non-hydrostatic stress field," *International Journal of Rock Mechanics and Mining Sciences & Geomechanics Abstracts*, 1988.
- [16] H. Stehfest, "Algorithm 368: numerical inversion of Laplace transforms," *Communications of the ACM*, vol. 13, no. 1, pp. 47–49, 1970.
- [17] B. S. Aadnoy and M. E. Chenevert, "Stability of highly inclined boreholes (includes associated papers 18596 and 18736)," *SPE Drilling Engineering*, vol. 2, no. 4, pp. 364–374, 1987.
- [18] R. T. Ewy, "Wellbore-stability predictions by use of a modified lade criterion," *SPE Drilling and Completion*, vol. 14, no. 2, pp. 85–91, 1999.